Temperature distribution in a permafrost-affected rock ridge from conductivity and induced polarization tomography

P.-A Duvillard, Florence Magnin, André Revil, A Legay, Ludovic Ravanel, F Abdulsamad, A Coperey

Temperature distribution in a permafrost-affected rock ridge from conductivity and induced polarization tomography

P.-A. Duvillard[1,2,3], F. Magnin[1], A. Revil[1], A. Legay[1], L. Ravanel[1], F. Abdulsamad[1], and A. Coperey[1]

1. EDYTEM, Univ. Savoie Mont-Blanc, Univ. Grenoble Alpes, CNRS, 73000 Chambery, France.
2. PACTE, Univ. Grenoble Alpes, CNRS, 38000 Grenoble, France.

Corresponding author: André Revil (andre.revil@univ-smb.fr)

Emails: pierre-allain.duvillard@univ-smb.fr; florence.magnin@univ-smb.fr; andre.revil@univ-smb.fr; ludovic.ravanel@univ-smb.fr; feras.abdul-samad@univ-smb.fr. antoine.coperey@univ-smb.fr; legay.alexandre@gmail.com

Key points: 1. Understanding the temperature distribution in a high Alpine rock ridge is a crucial step for hazard assessment. 2. Electrical conductivity and normalized chargeability are very sensitive to temperature in freezing conditions. 3. Electrical conductivity and induced polarization tomography can be used to provide temperature tomograms of a permafrost-affected rock ridge.

Keywords: high-Alpine rock ridge; electrical conductivity; freezing curve; permafrost.

Intended for publication in Geophysical Journal International

Abstract. Knowledge on the thermal state of steep alpine rock faces is crucial to assess potential geohazards associated with the degradation of permafrost. Temperature measurements at the rock surface or in boreholes are however expensive, invasive, and provide spatially-limited information. Electrical conductivity and induced polarization tomography can detect permafrost. We test here a recently-developed petrophysical model based on the use of an exponential freezing curve applied to both electrical conductivity and normalized chargeability to infer the distribution of temperature below the freezing temperature. We then apply this approach to obtain the temperature distribution from electrical conductivity and induced polarization field data obtained across a profile extending from the SE to NW faces of the lower Cosmiques ridge (Mont Blanc massif, Western European Alps, 3613 m a.s.l., France). The geophysical datasets were acquired both in 2016 and 2019. The results indicate that the only NE face of the rock ridge is frozen. To evaluate our results, we model the bedrock temperature across this rock ridge using CryoGRID2, a 1D MATLAB diffusive transient thermal model and surface temperature time series. The modelled temperature profile confirms the presence of permafrost in a way that is consistent with that obtained from the geophysical data. Our study offers a promising low-cost approach to monitor temperature distribution in Alpine rock walls and ridges in response to climate change.

1. Introduction

Permafrost is defined as ground materials with temperature permanently below or equal to the freezing temperature, which is typically around 0°C (Dobinski, 2011). Permafrost in mid latitude mountain areas is currently strongly affected by climate change (e.g., Biskaborn et al., 2019; PERMOS, 2019). In turn, permafrost degradation (warming and thawing of the ice content) is known to have serious consequences on the mechanical properties of the rock slopes (Gruber & Haeberli 2007; Krautblatter et al., 2013), resulting in an increasing rockfall frequency and magnitude that affects high mountain rock walls (Haeberli & Beniston, 1998; Ravanel & Deline, 2011; Ravanel et al., 2017). A precise knowledge of the thermal state of permafrost in rock walls and rock ridges is therefore crucial in assessing the safety and reliability of mountain infrastructures (Haeberli et al., 2010; Krautblatter et al., 2012), and to prevent or limit their damages or disturbances (Duvillard et al., 2019).

Rock wall temperature can be directly determined and monitored by the mean of temperature sensors installed at the rock surface or in boreholes (e.g., Magnin et al., 2015a). Since these data are local (point or line measurements), there are commonly used to fit statistical models explaining the rock surface temperature (e.g., Boeckli et al., 2012). They can be also used to parameterize or validate physic-based models (i.e., based on solving the heat equation) to infer the spatial distribution and evolution of rock wall permafrost and temperature when direct measurements are missing (e.g., Gruber et al., 2004; Magnin et al., 2017a; Magnin et al., 2019). However, the accuracy of the models is limited because of (i) a lack of consideration of important parameters driving the energy balance at the rock surface (e.g., variability in solar radiation or snow deposit), (ii) the rock material characteristics (e.g., the thermal conductivity, porosity, specific heat storage coefficient) are generally defined upon standard values, considered as homogenous and isotropic, and finally because (iii) complex heat transfer processes such as heat advection in bedrock fractures resulting of air circulation or water infiltration are neglected. That said, simplified thermal models have been shown to be reliable to estimate the permafrost characteristics at a given time period at depth > 8 m, and to estimate its changes over pluriannual time scales (Magnin et al., 2017).

To overcome some of the limits of direct temperature measurements and numerical modelling, electrical conductivity and induced polarization tomography can provide an alternative and complementary way to estimate the extent of permafrost and temperature distribution below the freezing temperature. In the past, electrical conductivity tomography has been broadly used to detect and monitor mountain permafrost (e.g., Kneisel, 2006; Krautblatter & Hauck, 2007; Supper et al., 2014; Mollaret et al., 2019) including in steep rock walls (Magnin et al., 2015b; Keuschnig et al., 2017). Indeed, the much lower electrical conductivity of frozen rocks with respect to unfrozen materials (see, for instance, Scott et al., 1990; Maurer & Hauck, 2007; Kneisel et al., 2008). The advantages of these geophysical methods are their low cost, their non-invasive character, and the fact that they provide 2D or 3D tomograms/images of the subsurface.

Krautblatter et al. (2010) and Magnin et al. (2015b) have been used laboratory experiments to distinguish frozen from unfrozen rocks based on their electrical conductivity. Currently, there is however an absence of a rigorous protocol to infer the temperature distribution from electrical conductivity tomography. To our knowledge, these limitations are due to the lack of a precise petrophysical-based methodology to infer temperature fields from electrical conductivity tomograms. The conversion of electrical conductivity into temperature distribution has however been successfully accomplished for other geological contexts than permafrost such as, for instance, active volcanoes (Revil et al., 2018). A similar strategy is followed in the present work.

In addition to electrical conductivity tomography, another geophysical method called induced polarization can be used to infer the presence of permafrost (e.g., Duvillard et al., 2018; Abdulsamad et al., 2019). Induced polarization refers to the reversible storage of electrical charges in a porous material under a low-frequency varying (applied) electrical field (e.g., Seigel, 1959; Kemna et al., 2012; Weller et al., 2013). In absence of metallic particles and in presence of moisture in a porous or fractured rock, induced polarization is related to the properties of the electrical double layer coating the surface of the grains (Revil, 2012, 2013; Leroy et al., 2017). Recently, the dynamic Stern layer concepts developed by Revil (2012, 2013) have been extended to freezing conditions (Duvillard et al., 2018; Coperey et al., 2018; Abdulsamad et al., 2019; Revil et al., 2019a). One of the advantages of induced polarization is that it can be measured with the same equipment as the one used for electrical conductivity data acquisition (Kemna et al., 2012).

The recent establishment of a unified petrophysical model describing both electrical conductivity and induced polarization (normalized chargeability) of rocks in freezing conditions provides the opportunity to convert electrical conductivity to temperature in areas affected by permafrost. Our study proposes to investigate the potential of these geophysical measurements and such petrophysical model tested on rock samples from outcrops to assess the temperature field patterns of a high-Alpine rock ridge. Then, we apply our approach to electrical conductivity and induced polarization data measured across the permafrost-affected lower Cosmiques ridge (3613 m a.s.l.), in the Mont Blanc massif (Western European Alps, France), below a refuge damaged by a 600-m^3-rockfall in August 1998 (Ravanel et al., 2013). To evaluate the results from the geophysical data, we use the rock surface temperature time series collected on each side of the ridge (from July 2016 to September 2019 on the north face and from July 2016 to April 2020 on the south face) to force a non-linear 1D heat conduction model simulating the temperature across a profile crossing the ridge. This modelling exercise is performed to see if the frozen portion of the ridge is consistent with the prediction from geophysics.

2. Petrophysics

2.1. Electrical conductivity - temperature relationship

Above the freezing temperature, the change in the electrical conductivity of a rock with temperature is controlled by the temperature dependence of the ionic mobilities, which is in turn controlled by the temperature dependence of the dynamic viscosity of the pore water. In these conditions, the temperature dependence of the electrical conductivity $\sigma(T)$ at temperature T (in S m^{-1}) is given by Revil et al. (2018):

$$\sigma(T) = \sigma(T_0)\left[1 + \alpha_T (T - T_0)\right], \tag{1}$$

where α_T = 0.021 °C^{-1} (i.e., the temperature dependence of the conductivity is roughly 2 % per degree Celcius, independent of the water content of the rock), the reference temperature is T_0 = 25°C, and $\sigma(T_0)$ denotes the conductivity of the rock at the reference temperature. The conductivity of a rock represents the ability of the rock to conduct an electrical current under the application of an electrical field. It comprises two contributions: a bulk contribution associated with conduction in the bulk pore space and a surface conductivity associated with conduction in the electrical double layer coating the surface of the grains. Usually, in a shallow temperature field above freezing conditions, the spatial variability associated with equation (1) (2% change per degree Celsius) is much smaller than the variability associated with the spatial variations in porosity, texture, and surface conductivity. It follows that above the freezing temperature, a single snapshot of the electrical conductivity distribution cannot be used to infer the temperature distribution.

In freezing conditions, part of the liquid pore water of a rock is progressively transformed into ice so there is also an additional effect associated with the change of the water content itself. Since the salt remains segregated in the liquid pore water, the salinity of the liquid pore water increases with the decrease of temperature. These effects imply a strong impact of the temperature on the electrical conductivity, an impact that is much stronger than above the freezing temperature. To quantitatively assess these effects, few ingredients are required. The most important is the expression of a freezing curve describing the relationship, for a given porous material, between the liquid water content θ (dimensionless) and the temperature T (in °C). In Duvillard et al. (2018) and Coperey et al. (2019), the following exponential freezing curve was proposed and validated:

$$\theta(T) = \begin{cases} (\phi - \theta_r)\exp\left(-\dfrac{T - T_F}{T_C}\right) + \theta_r, T \leq T_F \\ \phi, T > T_F \end{cases}, \quad (2)$$

where θ_r (dimensionless) denotes the residual water content when $T << T_F$, T_F denotes the liquidus or freezing point/temperature, T_C denotes a characteristic temperature controlling the transition between the unfrozen state and the frozen state, ϕ (dimensionless) denotes the (connected) porosity, and $\phi - \theta_r$ denotes the maximum volumetric ice content at low temperatures. Equation (2) is somehow equivalent to the capillary pressure curve in drainage and imbibition studies and the temperature T_C is somehow associated with the broadness of the pore size distribution.

In freezing conditions, the conductivity of the rock is given by Duvillard et al. (2018):

$$\sigma = \theta^{m-1} \frac{\sigma(T_0)}{\phi}\left[1 + \alpha_T (T - T_0)\right], \quad (3)$$

where m (dimensionless) denotes the cementation (porosity) exponent entering into Archie's law between the formation factor F and the porosity ϕ, i.e., $F = \phi^{-m}$. A typical value of m is close to 2 and a typical range is between 1.5 and 2.5 (e.g., Coperey et al., 2019, and references therein). In equation (3), we do not have to make any assumption regarding the importance of surface conductivity associated with the cation exchange capacity of the rock (see Duvillard et al., 2018; Coperey et al., 2019, for details regarding this contribution). The effect of temperature below freezing conditions upon the electrical conductivity is therefore very strong, much stronger than changes associated with porosity and surface conductivity spatial changes in a given lithology (Coperey et al., 2019).

Assuming that the cementation exponent m is close to 2, an explicit relationship is obtained between the measured conductivity below the freezing point, $\sigma(T)$, and temperature, T:

$$\sigma(T) \approx \left[(\phi - \theta_r) \exp\left(-\frac{T - T_F}{T_C} \right) + \theta_r \right] \frac{\sigma(T_0)}{\phi} \left[1 + \alpha_T (T - T_0) \right]. \tag{4}$$

Equation (4) will be used to connect electrical conductivity to temperature in field conditions. Below the freezing temperature, temperature spatial variations are expected to be mimicked, to some level, by the electrical conductivity distribution.

2.2. Normalized chargeability - temperature relationship

In the present paper, induced polarization is characterized by a single parameter called the normalized chargeability, which can be either obtained from the frequency dispersion of the conductivity data (for instance measured at two distinct frequencies, the so-called frequency effect) or from time-domain induced polarization by looking at the decay of the secondary voltage after the shut-down of the primary current (Kemna et al., 2012). Above the freezing temperature, the change in the normalized chargeability M_n (in S m^{-1}) of a rock with temperature is controlled by the temperature dependence of the ionic mobilities, which is in turn controlled by the temperature dependence of the dynamic viscosity of the pore water. Like for the electrical conductivity, we have therefore (Revil et al., 2012):

$$M_n(T) = M_n(T_0)\left[1 + \alpha_T (T - T_0)\right], \tag{5}$$

where α_T = 0.021 °C^{-1}, the reference temperature is T_0 = 25°C, and $M_n(T_0)$ denotes the normalized chargeability of the rock at the reference temperature. Using the model developed in Duvillard et al. (2018), the dependence of the normalized chargeability in freezing conditions is given by:

$$M_n(T) \approx \left[(\phi - \theta_r)\exp\left(-\frac{T - T_F}{T_C} \right) + \theta_r \right] \frac{M_n(T_0)}{\phi} \left[1 + \alpha_T (T - T_0)\right]. \tag{6}$$

Therefore, in freezing conditions, the temperature dependence of the normalized chargeability and the temperature dependence of the electrical conductivity are strictly the same. This is because of the specific dependence of the conductivity with the water content in freezing conditions related to the segregation of salt in the liquid water phase. Thus, at the opposite of what can be done in hydrothermal systems (Revil et al., 2019b), we cannot combine here the normalized chargeability and electrical conductivity tomography to obtain independently the liquid water content.

Interestingly however, the ratio of the normalized chargeability by the conductivity appears to be independent of temperature and, from equations (4) and (6), we have:

$$\frac{M_n(T)}{\sigma(T)} \approx \frac{M_n(T_0)}{\sigma(T_0)}. \tag{7}$$

According to the dynamic Stern layer model developed by Revil (2012) and for conditions implying that the salt remains segregated into the liquid pore water, the normalized chargeability and the conductivity are related to the water content θ by

$$M_n(T_0) \approx \theta^{m-1} \rho_g \lambda \text{CEC}, \tag{8}$$

$$\sigma(T_0) \approx \theta^{m-1} \sigma_w + \theta^{m-1} \rho_g B \text{CEC}, \tag{9}$$

respectively. Therefore, the ratio between the normalized chargeability and the conductivity is given by

$$\frac{M_n(T)}{\sigma(T)} \approx \frac{\rho_g \lambda \mathrm{CEC}}{\sigma_w + \rho_g B \mathrm{CEC}} . \quad (10)$$

When the conductivity of the rock is dominated by surface conductivity along the surface of the grains (i.e., $\sigma_w << \rho_g B\mathrm{CEC}$), this ratio is exactly given by $R = \lambda / B = 0.10$, independent of the water content and temperature (Duvillard et al., 2018). When we have $M_n(T)/\sigma(T) < R$, this means that the bulk contribution of electrical conductivity (related to the pore water conduction σ_w) cannot be neglected.

3. Test site

The lower Cosmiques ridge is located at 600–1000 m SSW of the Aiguille du Midi (3842 m a.s.l.), on the northwestern side of the Mont Blanc massif (Figure 1a), which spreads between France, Italy and Switzerland, and belongs to the Alpine external crystalline massifs. The ridge develops horizontally, on the French side of the massif, over a length of 400 m (Figure 1bc) in the Mont Blanc granite from the Hercynian metamorphic series (Bussy and von Raumer, 1994). The extension of the SE face is 50-m-high and stands above the Glacier du Géant. It is about 75° steep and has a rather smooth surface. It is sometimes partially covered by the snow that takes support on the glacier below. The NW face is about 350-m-high, 55° steep, and is highly rugged, allowing heterogeneous snow accumulation during a part of the year. The Mean Annual Rock Surface Temperature (MARST), modeled for the steep slopes of the Mont Blanc massif for the period 1961-1990 (Magnin et al., 2015c), is around -4°C in the NW face, and -1°C in the SE face of the lower Cosmiques ridge. A refuge was built during the period 1989 - 1991 on the top of the ridge (3613 m a.s.l.). It represents a popular location (hosting about 7000 people a year) since it is located along one of the main climbing route to reach the summit of the Mont Blanc. In August 1998, a 600 m^3-rockfall occurred right below the refuge and partly destabilized the infrastructure, which was closed for 8 months for reinforcement work (Figure 1d; Ravanel et al., 2013).

4. Methods

4.1. Geophysical measurements

4.1.1 Field investigations

The geophysical field survey was performed both in October 2016 and September 2019. It extends from the foot of the SE face to the upper 64 m of the NW face, running below the refuge anchors and building (Figure 2). Two 64-m-long cables (128-m-long profile) and a total of 64 electrodes (2-m-spacing) were connected to a resistivity meter (ABEM Terrameter SAS-4000 in 2016 and ABEM LS2 in 2019). We used 10-mm-thick and 120-mm-long stainless steel electrodes for both surveys. Warm salty water, conductive metallic grease, and bentonite were used to improve the electrical contacts between the electrodes and the ground (Krautblatter & Hauck, 2007; Magnin et al., 2015b). The Wenner configuration was used because of its best signal-to-noise ratio thanks to its particular electrode configuration since the voltage electrodes MN are located in-between the current electrodes AB (e.g., Dahlin and Zhou, 2004; Kneisel, 2006). During the surveys, only two electrodes had to be excluded due to their high contact resistances (Table 1). Topography along the profile was extracted from a terrestrial laser scanning point cloud acquired in 2016 for the SE face and from a photogrammetric model acquired with a drone in 2019 on the both faces of the ridge. The data were inverted with the RES2DINV-3.54.44 software using a smoothness-constrained least-squares method and the standard Gauss-Newton method (see Loke and Barker, 1996, for details). The inversion was stopped at the 3rd iteration when the convergence criterion was reached (i.e., the difference in the root-mean square error of the data misfit function is below a target value).

4.1.2. Laboratory experiments

In order to test the petrophysical model discussed in Section 2, we performed an electrical conductivity experiment on a rock sample collected in the field from an outcrop. The sample (labeled PAS1 below) was immersed in a temperature-controlled bath following the same protocol as in Duvillard et al. (2018). Sample PAS1 was cut to get a 5-cm large cube. Sample PAS1 (granite) was characterized by a porosity ϕ = 0.028, a cation exchange capacity CEC = 0.80 meq/100 g, and a formation factor F = 499 (for more details, see sample labelled COS in Coperey et al., 2019). Before to perform the laboratory measurements in the laboratory, the sample was dried during 24 hours then saturated under vaccuum with degassed water from melted snow taken on the field. The sample was left several weeks in the solution to reach chemical equilibrium before to perform the laboratory measurements. The water conductivity at 25˚C and at equilibrium was 0.0257 S m^{-1}.

In addition, we used the laboratory data determined by Magnin et al. (2015b). This second sample (labeled G1 below) was collected in the same geological unit and saturated with tap water. Four non-polarizing Ag-$AgCl_2$ electrodes were placed on the sample: two current electrodes (A and B) on the end-faces of the sample. Two voltage electrodes (M and N, separated by a distance of 3.5 cm) were placed on the external side of the core sample.

The sample holder was installed in a heat-resistant insulating bag immersed in a thermostat bath (KISS K6 from Huber; 210 × 400 × 546 mm; bath volume: 4.5 L). The temperature of this bath was controlled with a precision of 0.1°C. Glycol was used as heat carrying fluid and the complex conductivity measurements were carried out with the impedance-meter. The conductivity measurements were reported here at 1 Hertz. The experimental data together with a fit of the data with equation (1) (for temperatures above the freezing temperature) and with equation (4) (for temperatures below the freezing temperature) are shown in Figure 3. We see that the model proposed in Section 2 is able to fit the data above and below the freezing temperature and provides therefore a bridge to connect electrical conductivity to temperature.

Induced polarization measurements were done in time domain with the sample core I.P. tester from GDD Inc. and using sample Sample PAS1. We used the four electrodes approach, i.e., current electrodes A and B are attached on the end faces of the cyclindrical core while the potential electrodes M and N are fixed on the external side of the sample. In order to avoid drying and short circuits at the electrodes, the sample was covered with insulating adhesive tape except at the position of the electrodes. Then, the sample was brought to different temperatures thanks to a thermally-controlled bath (Kiss K6 from Huber; see Figure 5 in Coperey et al., 2019). The periods of the primary current injection were 1.0, 2.0 and 4.0 seconds. The decay curve was recorded using 20 windows distributed in a "Cole-Cole" configuration. More details about time-domain induced polarization measurements can be found in Kemna et al. (2012) and Revil et al. (2018). The results are shown in Figure 4 and are fitted by equations (5) and (6). We see that the model is able to fit the data very well.

In our analyzis, from Figure 3, we have $M_n(T_0)$ = 5.9×10^{-7} S m^{-1} and from Figure 4 we have $\sigma(T_0)$ ≈ 9×10^{-5} S m^{-1}. This yields $M_n(T)/\sigma(T)$ = 0.007 << R, which means in turn that surface conduction is not the dominating conduction mechanisms controlling the electrical conductivity of these rocks. Unaltered granite rock samples are usually characterized by a low specific surface areas and CEC, which could explain this observation.

4.2 Rock surface temperature measurement and temperature modeling

Rock surface temperature (RST) measurements allow to locally assessing the presence of permafrost by continuously measuring temperature for at least one full year (Gruber et al., 2004; Magnin et al., 2015a). Three RST sensors Geoprecision PT1000 with M-Log5W loggers (resolution: 0.01°C, accuracy +/- 0,1°C with temperature recorded every 3 hours) were installed at a depth of 10 cm in July 2016 in the SE and NW faces and near the refuge foundation. The latter is not used in this study. The SE face sensor was installed 15 m below the refuge (at 3595 m a.s.l.), in the 1998 scar, and the NW face sensor was installed below the terrace of the refuge (at 3603 m a.s.l.) in a massive slab (Figure 2). The NW face sensor was installed in a snow-free location, but the one on the SE face was installed on a rock wall on which snow accumulates in winter, covering the sensor. These sensors recorded RST at an hourly time step until September 2018 yielding time series > 2 years. The MARSTs allow a first approximation of the presence/absence of permafrost, negative values indicating the very likely presence of permafrost while values up to 3°C might also indicate possible permafrost presence (Hasler et al., 2011). Such data can also be used to simulate permafrost evolution at depth by forcing a heat conduction model (e.g., Hipp et al., 2014).

To evaluate the occurrence of permafrost obtained from field electrical conductivity measurements, we simulate the bedrock temperature evolution during the years prior to measurements in order to assess the thermal state at the day of geophysical investigations in 2016 and 2019. To do so, we first reconstruct a time series of the daily RST (January 1993 to July 2016) at the SE and NW loggers locations by fitting a linear regression model between the measured RST and local air temperature records (data from *Météo France*). We tested the model fit with air temperature records from Chamonix (1042 m a.s.l.) and the Aiguille du Midi (3842 m a.s.l.). The best correlation between daily RST and daily air temperature was obtained with the Chamonix time series for the NW sensor (0.88) and with the Aiguille du Midi time series for the SE sensor (0.77 against 0.63 for the Chamonix time series). Lower correlation between air temperature and RST on at the SE sensor is due to the presence of snow during winter and the stronger variability in incoming solar radiation than at the NW sensor.

We then used air temperature time series best correlated with the RST to reconstruct the RST prior to and after RST measurements by using the fitted regression model coefficients. Since the Aiguille du Midi weather records only start in February 2007 and because they are affected by several gaps during the period 2007-2019, data from the Chamonix time series, which are continuous over time, were used to fill the gaps when reconstructing the RST time series on the SE face. Two RST time series are thus created for the NW and SE logger locations, starting in January 1993 (beginning of the continuous air temperature measurements by *Météo France* in Chamonix) and ending in September 2019, with the measured values between July 2016 and September 2018 and the reconstructed values before and after. These time series were used to force a MATLAB diffusive transient thermal model, the so-called Cryogrid 2 model (Westerman et al., 2013).

We solve a 1D nonlinear diffusion equation over time by taking into account rock properties, air content, water/ice content, and related thawing/freezing processes through latent heat consumption and release. Our goal is to determine the temperature distribution along a quasi-horizontal profile crossing the ridge with a length of 32.75 m. In the original approach by Westerman et al. (2013), Cryogrid2 is used to model the temperature distribution in a vertical section with only the upper surface that has been exposed to air. Therefore, a RST time series is used to impose the boundary condition at the top of the column (corresponding therefore to a Dirichlet boundary condition) and a thermal flux at the bottom (corresponding to a Neumann boundary condition).

Our model is however different from the modeling used in Westerman et al., (2013) since we model the temperature distribution across a ridge and we need to apply two RST time series (the SE and NW temperature time series) at both ends of the profile. In other words, in our case, we apply a Dirichlet boundary condition at each end of the 1D profile to estimate the temperature distribution by solving the heat equation with Cryogrid2.

The equations are solved with a spatial resolution of 10 cm near the two end-points (i.e., from 0 to 1 m and from 31.75 to 32.75 m). We use a discretization of 20 cm in the remaining part of the profile (i.e., from 1 to 31.75 m). The simulation is performed between 1993 January 1st and 2019 September 18th. Physical rock parameters were fitted using temperature time series in three 10-m-depth boreholes at the Aiguille du Midi (Magnin et al., 2015a). They are reported in Table 2 and provide reasonable estimates for granites.

Legay et al. (submitted) have calculated model uncertainty (standard deviation) of 0.55°C according to the error distribution (difference between the modeled and measured temperature values in the boreholes). In addition, uncertainties of the inputs of the model must be considered; the loggers give an uncertainty of $\Delta_{95\%}$ = 1.1°C for the measured temperatures time series (NW and SE series).

5. Results

5.1. Electrical conductivity and normalized chargeability tomograms

Electrical conductivity tomograms acquired in 2016 and 2019 show a vertical distribution of the conductivities with rather low conductivity values (< 10^{-4} S m^{-1}) below the NW face and higher values below the SE face (> 10^{-4} S m^{-1}). The chargeability tomograms acquired in 2019 show a similar vertical distribution between the NW face and SE face with lower values in the NW face compared to 2016 (>10^{-6} S.m^{-1}). The two color scales are adjusted with 0°C value to the conductivity values (between 10^{-4} S.m^{1} and 10^{-5} S.m^{1}) or normalized chargeability values (between 10^{-6} S.m^{1} and 10^{-7} S.m^{1}) observed during the laboratory experiments (Figures 3 and 4). This suggests that permafrost presence is restricted to the NW face with a vertical permafrost limit below the hut and the absence of permafrost below the SE face (Figures 5 and 6). At this stage, only a semi-quantitative interpretation of the profiles is possible, as previously carried out in previous studies analyzing electrical conductivity tomograms in rock walls (Krautblatter & Hauck, 2007; Magnin et al., 2015b; Keuschnig et al., 2017). This is, at the current stage, not possible to assess how close to the thawing point the permafrost is.

5.2. Petrophysical modelled temperature distribution in the ridge

In order to convert the electrical conductivity distribution into temperature fields, we consider the following values of the model parameters entering equations (4): T_C =-0.36°C, ϕ = 0.028, θ_r = 0.006, $T_F = 0°\text{C}$ based on the experimental data (Figure 3). In addition, we consider the characteristic temperature entering equation (4) in the range $-2.2°\text{C} \le T_C \le -0.4°\text{C}$ based on our experimental data. The last step is to determine the value of the conductivity of the rock at the reference temperature, i.e., $\sigma(T_0)$. We first determine the value of $\sigma(T_F = 0°\text{C})$ from the electrical conductivity distribution resulting from the electrical conductivity tomogram. This value is obtained as follows. Because of the change of slope in the conductivity versus temperature curve, the distribution of the conductivity values should be marked by a minimum, which is clearly identified in Figures 7 and 8 for both laboratory and field data, acquired in 2016 and 2019. This yields $\sigma(T_F = 0°\text{C}) = 5\times10^{-5}$ S.m^{-1} for the field data. Then, this value is converted to the reference temperature of 25°C to be used in equation (4). Using equation (1), we obtain $\sigma(T_0)$ = 8×10^{-5} S m^{-1}, therefore in excellent agreement with the values determined independently from the curve fitting shown in Figure 3 ($\sigma(T_0)$ = 8.8×10^{-5} S.m^{-1} for sample G1 and $\sigma(T_0)$ = 9.3×10^{-5} S.m^{-1} for sample PAS1). This indicates that the two samples are representative of the rock below the Cosmiques refuge since the value of this conductivity is consistent between laboratory and field data.

With these values, two temperature distributions are shown in Figure 9 for $T_C = -2.2°\mathrm{C}$ and $T_C = -0.4°\mathrm{C}$, respectively. These results show a relative increase of the lowest temperature between 2016 and 2019, according to the two sample (sample G1, -1.7°C in 2016, then -1°C in 2019; sample PAS1, -10°C in 2016, then -6°C in 2019), suggesting permafrost degradation (warming) within this 3 year period.

5.3 Measured and modelled bedrock temperature

The MARST during the measurement period (from August 15, 2016 to August 15, 2018) was -3.7°C on the NW face and +2.4°C on the SE face. This is in agreement with suggestion from the petrophysical models which displays permafrost conditions below the NW face but not below the SE face. Temperatures simulated at depth with CryoGRID2 are presented in Figure 10 for the period from 2009 January 1st to 2019 September 18th. They show a depth of the permafrost in the NW face around -15 m with temperature between -2/-3°C during the ERT and IP acquisition in October 2016 and September 2019. This simulation indicates warm permafrost in the NW face, probably in thawing phase.

6. Discussion

6.1 Comparison between geophysics and numerical modeling

When we compare the negative temperature converted from the geophysics (petrophysical model only used under 0°C) with temperature simulated with the numerical model, we observe that the NW face of the rock ridge is frozen with both methods, in 2016 and 2019. We recall that the geophysical data can only be used to assess the temperature in the frozen portion of the ridge; above the freezing temperature, the effect of heterogeneity is stronger than the effect of temperature regarding their effects on the conductivity field. Figure 9 confirms a good correlation between the frozen and unfrozen part of the ridge between the geophysical prediction and the numerical modeling. The temperature distribution with T_c = -2.2°C (sample PAS1 saturated with snowmelt; Figure 3a) suggests that the bedrock temperature is between -2°C and -4°C in 2016 and 2019 at a depth of 10 m in the NW face while the temperatures simulated with the numerical model is -2°C. The determination of the temperature distribution assuming T_c = -0.36°C (Figure 3b) suggests a bedrock temperature of -0.5°C at 10 m depth in 2016 and 2019 while the numerical simulation suggests -2°C. Therefore, the numerical modeling shows that the NW face of the rock ridge is frozen (permafrost conditions) with a temperature around -2°C; which is very consistent with the interpretation of the geophysical data from the sample PAS1 (with T_c = -2.2°C, see Figure 9).

6.2 Uncertainty

In the previous section, we made a qualitative comparison between the prediction of the geophysical data using the petrophysical model discussed in Section 2 and the 1D numerical model. We avoided a direct comparison because, in our opinion, both approaches contain sources of uncertainties. For the numerical model, the main sources of errors are associated with (1) uncertainties associated with the dimensionality of the numerical model, (2) uncertainties in the value of the petrophysical parameters used in the heat equation, (3) uncertainties in the boundary conditions, and (4) uncertainties in the numerical modeling itself. Regarding the geophysical data, sources of errors are associated with (1) uncertainties in the inversion of the geophysical data (choice of the regularization term in the cost function), (2) uncertainties in the geophysical data, and (3) uncertainties in the parameters entering in the petrophysical model. A complete analyzis of the uncertainties associated with the two approaches is out of the scope of the present paper. This being said, a future investigation will focus on a temperature tomogram that will combine 2D numerical modeling of the heat equation with the geophysical data to get a balance in terms of combining the two types of information.

6.3 Influence of surface conductivity

In absence of metallic particles, the electrical conductivity of a rock sample has two contributions: a bulk conductivity associated with the pore water in the connected pore space and a surface (interfacial) conductivity associated with conduction in the electrical double layer coating the surface of the grains. The third point we want to discuss is the influence of this surface conductivity in the overall electrical conductivity of the rock ridge. With the laboratory data, we already demonstrated that surface conduction is likely not dominant in explaining the conductivity of the granite from the ridge. What about the field data? Figure 11 displays the field and laboratory data in terms of normalized chargeability versus conductivity. It clearly shows that the slope ($0.016 \ll R = 0.10$) is such that the conductivity is dominated with the pore water conductivity rather than by the surface conductivity. This is an important point in interpreting electrical conductivity tomograms in field conditions.

7. Conclusions

Assessing permafrost distribution in steep high-Alpine rock walls and ridges is challenging due to the highly variable temperature distribution, largely governed by the micro- to meso-topographical settings and the related topoclimatic control. Point-scale temperature measurements and temperature models are therefore limited. In this study, we proposed to assess the 2D temperature distribution of a sensitive rock ridge (presence of a refuge with 140 beds) by mean of an electrical conductivity tomography measurement and a petrophysical model parameterized with calibrated freezing curves in laboratory. The electrical conductivity data performed on two rock samples were used for these calibrations and fitted with the petrophysical model developed in Duvillard et al. (2018). The parameterized petrophysical model applied to electrical conductivity data performed over the rock ridge provides realistic temperature fields for the lower Cosmiques ridge. Warm permafrost is inferred right below the NW face and the absence of permafrost is inferred right below the SE face and below the refuge. The resulting temperature extracted from geophysics, with sample saturated with melted snow, advert temperature around -2°C, which is consistent with the simulated temperature. This approach needs to be tested on other areas to better assess the asset and limits of the proposed method. An in-depth analyzis of the relationship between the conductivity and the normalized chargeability indicates that the conductivity is dominated here by the bulk conductivity rather than by the surface conductivity associated with conduction in the electrical double later coating the grains.

Acknowledgments. This research is part of the FEDER POIA "PermaRisk" project. P.-A. Duvillard's PhD fellowship was supported by a grant from *Ingénierie des Mouvements du Sol et des Risques Naturels* (IMSRN) and the *Association Nationale de la Recherche et de la Technologie* (ANRt). P.-A. Duvillard's Post-doc is supported by a grant from FEREC foundation by the STAAF project. Authors thank E. Mallet, M. Marcer, M. Rameau, C. Mörtl and G. Marsy for their help on the field. We thank E. Veyrat-Durebex and L. Ravanel, the two successive keepers of the Cosmiques refuge, as well as the alpine guides of the *Compagnie des Guides de Chamonix* for sharing their knowledge of the area. We thank A. Soueid Ahmed, G. Menard, and M. Mallet for fruitful discussions on the topic of the present paper. The data used in this study will be available upon the publication of this paper on ResearchGate. The work of A. Revil is supported by I-RISK, Indura, and the Région Auvergne-Rhône-Alpes.

References

Abdulsamad F., Revil A., Ghorbani A., Toy V., Kirilova M., Coperey A., Duvillard P.A., Ménard G. & Ravanel L., 2019. Complex conductivity of graphitic schists and sandstones, *Journal of Geophysical Research*, **124**, 8223–8249, doi:10.1029/2019JB017628

Biskaborn B.K., Smith S.L., Noetzli J., Matthes H., Vieira G., Streletskiy D.A., Schoeneich P., Romanovsky V.E., Lewkowicz A.G., Abramov A., Allard M., Boike J., Cable W.L., Christiansen H.H., Delaloye R., Diekmann B., Drozdov D., Etzelmüller B., Grosse G., Guglielmin M., Ingeman-Nielsen T., Isaksen K., Ishikawa M., Johansson M., Johannsson H., Joo A., Kaverin D., Kholodov A., Konstantinov P., Kröger T., Lambiel C., Lanckman J.-P., Luo D., Malkova G., Meiklejohn I., Moskalenko N., Oliva M., Phillips M., Ramos M., Sannel A.B.K., Sergeev D., Seybold C., Skryabin P., Vasiliev A., Wu Q., Yoshikawa K., Zheleznyak M., Lantuit H., 2019. Permafrost is warming at a global scale. *Nature Communications*, **10**, doi:10.1038/s41467-018-08240-4

Boeckli, L., Brenning, A., Gruber, S. & Noetzli, J., 2012. Permafrost distribution in the European Alps: calculation and evaluation of an index map and summary statistics, *The Cryosphere*, **6**, 807–820, doi:10.5194/tc-6-807-2012.

Bussy F., & von Raumer J.F. (1994). U-Pb geochronology of Palezoic magmatic events in the Mont-Blanc crystalline massif, Western Alps. *Swiss Bulletin of Mineralogy and Petrology*, **74**: 514-515.

Coperey, A., Revil, A., Abdulsamad, F., Stutz, B., Duvillard, P.A, Ravanel, L., 2019. Low frequency induced polarization of porous media undergoing freezing: preliminary observations and modeling. *J. Geophys. Res.*, **124**, doi:10.1029/2018JB017015.

Dahlin, T. & Zhou, B., 2004. A numerical comparison of 2D resistivity imaging with 10 electrode arrays, *Geophysical Prospecting*, **52**, 379–398, doi:10.1111/j.1365-2478.2004.00423.x.

Dobinski, W., 2011. Permafrost, Earth Science Review, **108**, 158–169, doi:10.1016/j.earscirev.2011.06.007.

Duvillard, P.A., Revil, A., Qi, Y., Soueid Ahmed, A., Coperey, A. & Ravanel, L., 2018. Three-dimensional electrical conductivity and induced polarization tomography of a rock glacier, *J. Geophys. Res.*, **123**, doi:10.1029/2018JB015965

Duvillard, P.-A., Ravanel, L., Marcer, M. & Schoeneich, P., 2019. Recent evolution of damage to infrastructure on permafrost in the French Alps, *Regional Environmental Change*, **19**, 1281-1293, doi:10.1007/s10113-019-01465-z

Gruber, S. & Haeberli, W., 2007. Permafrost in steep bedrock slopes and its temperature-related destabilization following climate change, *J. Geophys. Res*. **112**, doi:10.1029/2006JF000547.

Gruber, S., Hoelzle, M. & Haeberli, W., 2004. Rock-wall temperatures in the Alps: modelling their topographic distribution and regional differences, *Permafrost and Periglacial Processes*, **15**, 299–307, doi:10.1002/ppp.501.

Haeberli, W. & Beniston, M., 1998. Climate change and its impacts on glaciers and permafrost in the Alps, *Ambio*, **27**, 258–265.

Haeberli, W., Noetzli, J., Arenson, L., Delaloye, R., Gärtner-Roer, I., Gruber, S., Isaksen, K., Kneisel, C., Krautblatter, M. & Phillips, M., 2010. Mountain permafrost: development and challenges of a young research field, *Journal of Glaciology*, **56**, 1043–1058.

Kemna, A., Binley, A., Cassiani, G., Niederleithinger, E., Revil, A., Slater, L., Williams, K.H., Orozco, A.F., Haegel, F.-H., & Hoerdt, A., 2012. An overview of the spectral induced polarization method for near-surface applications. *Near Surface Geophysics*, **10**, 453–468. doi:10.3997/1873-0604.2012027.

Keuschnig, M., Krautblatter, M., Hartmeyer, I., Fuss, C. & Schrott, L., 2017. Automated electrical resistivity tomography testing for early warning in unstable permafrost rock walls around Alpine infrastructure, *Permafrost and Periglacial Processes*. **28**, 158–171. https://doi.org/10.1002/ppp.1916

Kneisel, C., 2006. Assessment of subsurface lithology in mountain environments using 2D resistivity imaging, *Geomorphology***, 80**, 32–44, doi:10.1016/j.geomorph.2005.09.012.

Kneisel, C., Hauck, C., Fortier, R. & Moorman, B. (2008) Advances in geophysical methods for permafrost investigations. *Permafrost Periglac. Process.*, **19**, 157–178. doi:10.1002/ppp.616

Krautblatter, M. & Hauck, C., 2007. Electrical resistivity tomography monitoring of permafrost in solid rock walls, *J. Geophys. Res*., **112**, doi:10.1029/2006JF000546.

Krautblatter, M., Verleysdonk, S., Flores-Orozco & A., Kemna, A., 2010. Temperature-calibrated imaging of seasonal changes in permafrost rock walls by quantitative electrical resistivity tomography (Zugspitze, German/Austrian Alps), *J. Geophys. Res.*, **115**, doi:10.1029/2008JF001209.

Krautblatter, M., Huggel, C., Deline, P. & Hasler, A., 2012. Research perspectives on unstable high-alpine bedrock permafrost: Measurement, modelling and process understanding, *Permafrost and Periglacial Processes,* **23**, 80–88, doi:10.1002/ppp.740.

Legay, A., Magnin, F., Ravanel L., submitted. Rock temperature prior to failure: analysis of 209 rockfall events in the Mont Blanc massif (Western European Alps), submitted to *Permafrost and Periglacial Processes*

Leroy, P., S. Li, Jougnot D., Revil A. & Wu Y., 2017. Modeling the evolution of spectral induced polarization during calcite precipitation on glass beads, *Geophysical Journal International*, **209**(1), 123-140, doi:10.1093/gji/ggx001.

Loke, M.H. & Barker, R.D., 1996. Rapid least-squares inversion of apparent resistivity pseudosections by a quasi-Newton method, *Geophysical Prospecting*, **44**, 131–152. doi:10.1111/j.1365-2478.1996.tb00142.x

Magnin, F., Deline, P., Ravanel, L., Noetzli, J. & Pogliotti, P., 2015a. Thermal characteristics of permafrost in the steep alpine rock walls of the Aiguille du Midi (Mont Blanc Massif, 3842 m a.s.l), *The Cryosphere*, **9**, 109–121, doi:10.5194/tc-9-109-2015

Magnin, F., Krautblatter, M., Deline, P., Ravanel, L., Malet, E. & Bevington, A., 2015b. Determination of warm, sensitive permafrost areas in near-vertical rockwalls and evaluation of distributed models by electrical resistivity tomography, *J. Geophys. Res*., **120**, 745–762, doi.org/10.1002/2014JF003351

Magnin, F., Brenning, A., Bodin, X., Deline, P. & Ravanel, L., 2015c. Modélisation statistique de la distribution du permafrost de paroi: application au massif du Mont Blanc, *Géomorphologie Relief Process. Environ*., **21**, 145–162.

Magnin, F., Josnin, J.-Y., Ravanel, L., Pergaud, J., Pohl, B. & Deline, P., 2017a. Modelling rock wall permafrost degradation in the Mont Blanc massif from the LIA to the end of the 21st century, *The Cryosphere*, **11**, 1813–1834, doi:10.5194/tc-11-1813-2017

Magnin, F., Westermann, S., Pogliotti, P., Ravanel, L., Deline, P., & Malet, E., 2017b. Snow control on active layer thickness in steep alpine rock walls (Aiguille du Midi, 3842 m a.s.l., Mont Blanc massif), *Catena*, **149**(2), 648–662, doi:10.1016/j.catena.2016.06.006.

Magnin, F., Etzelmüller, B., Westermann, S., Isaksen, K., Hilger, P. & Hermanns, R. L., 2019: Permafrost distribution in steep rock slopes in Norway: measurements, statistical modelling and implications for geomorphological processes, *Earth Surf. Dynam*., **7**, 1019–1040, doi:10.5194/esurf-7-1019-2019

Maurer, H. & Hauck, C. (2007) Geophysical imaging of alpine rock glaciers. *Journal of Glaciology*, **53**, 110–120. doi:10.3189/172756507781833893

Mollaret, C., Hilbich, C., Pellet, C., Flores-Orozco, A., Delaloye, R. & Hauck, C., 2019. Mountain permafrost degradation documented through a network of permanent electrical resistivity tomography sites, *The Cryosphere*, **13**, 2557–2578, doi:10.5194/tc-13-2557.

Noetzli, J., Gruber, S., Kohl, T., Salzmann, N. & Haeberli, W., 2007. Three-dimensional distribution and evolution of permafrost temperatures in idealized high-mountain topography, *Journal of Geophysical Research*, **112**(F2), doi:10.1029/2006JF000545.

PERMOS 2019. Permafrost in Switzerland 2014/2015 to 2017/2018. Noetzli, J., Pellet, C., and Staub, B. (eds.), Glaciological Report (Permafrost) No. 16-19 of the C*ryospheric Commission of the Swiss Academy of Sciences*, 104 pp, doi:10.13093/permos-rep-2019-16-1

Ravanel, L. & Deline, P., 2011. Climate influence on rockfalls in high-Alpine steep rockwalls: The north side of the Aiguilles de Chamonix (Mont Blanc massif) since the end of the 'Little Ice Age', *The Holocene*, **21**, 357–365. doi:10.1177/0959683610374887.

Ravanel, L., Deline, P., Lambiel, C. & Vincent, C., 2013. Instability of a high alpine rock ridge: the lower arête des cosmiques, mont blanc massif, france, *Geogr. Ann. Ser. Phys. Geogr.*, **95**, 51–66, doi:10.1111/geoa.12000.

Ravanel, L., Magnin, F. & Deline, P., 2017. Impacts of the 2003 and 2015 summer heatwaves on permafrost-affected rock-walls in the Mont Blanc massif, *Sci. Total Environ*., **609**, 132–143, doi:10.1016/j.scitotenv.2017.07.055.

Revil A., Razdan M., Julien S., Coperey A., Mao D., Abdulsamad F., Gasquet D., Sharma R. & Rossi M., 2019a. Induced polarization response of porous media with metallic particles

– Part 9. Influence of permafrost, *Geophysics*, **84**(5), A43-W32, doi:10.1190/geo2019-0013.1.

Revil A., Qi Y., Ghorbani A., Coperey A., Soueid Ahmed A., Finizola A. & T. Ricci, 2019b. Induced polarization of volcanic rocks. 3. Imaging clay cap properties in geothermal fields, *Geophysical Journal International*, **218**, 2, 1398–1427, doi:10.1093/gji/ggz207.

Revil A., Ghorbani A., Gailler L.S., Gresse M., Panwar N., & Sharma R., 2018. Electrical conductivity and induced polarization investigations at Kilauea volcano, Hawai'i, *Journal of Volcanology and Geothermal Research*, **368**, 31–50, doi:10.1016/j.jvolgeores.2018.10.014.

Revil, A, 2013. Effective conductivity and permittivity of unsaturated porous materials in the frequency range 1 mHz–1GHz, *Water Resources Research* **49**, 306–327, doi:10.1029/2012WR012700.

Revil, A., 2012. Spectral induced polarization of shaly sands: Influence of the electrical double layer, *Water Resources Research*, **48**, doi: 10.1029/2011WR011260.

Scott, W., Sellmann, P. & Hunter, J. (1990). Geophysics in the Study of Permafrost. in Geotechnical and Environmental Geophysics Investigations in Geophysics, Vols 1-0, 355–384, *Society of Exploration Geophysicists*. doi:10.1190/1.9781560802785.ch13

Seigel, H.O., 1959. Mathematical formulation and type curves for induced polarization, *Geophysics*, **24**, 547–565, doi:10.1190/1.1438625.

Supper, R., Ottowitz, D., Jochum, B., Römer, A., Pfeiler, S., Gruber, S., Keuschnig, M. & Ita, A., 2014. Geoelectrical monitoring of frozen ground and permafrost in alpine areas: field studies and considerations towards an improved measuring technology, *Surf. Geophys*. **12**, doi:10.3997/1873-0604.2013057.

Weller, A., Slater, L., & Nordsiek, S., 2013. On the relationship between induced polarization and surface conductivity: Implications for petrophysical interpretation of electrical measurements, *Geophysics*, **78**, D315–D325. doi:10.1190/geo2013-0076.1.

Westermann, S, Schuler, TV, Gisnås, K & Etzelmüller, B, 2013. Transient thermal modeling of permafrost conditions in Southern Norway, *The Cryosphere*, **7**(2), 719-739, doi:10.5194/tc-7-719-2013.

Tables

Table 1. Information regarding the electrical resistivity and induced polarization surveys. ER and IP stand for electrical resistivity and induced polarization, respectively.

Profile	ER2016	ER2019	IP2019
Date of survey	5 October	19 September	19 September
Electrode array type	Wenner 64XL	Wenner 64	Wenner 64
Number of data points	593	447	443
Number of inverted points	588	439	226
Root-mean-square error	29.5	19.2	14.2

Table 1: Parameters used for the numerical simulation of the ridge temperature according to the model Legay et al. (submitted). The value of these petrophysical parameters have been fitted using the temperature data measured in three shallow wells.

Parameter	Value
Thermal conductivity	3.3 W K^{-1} K^{-1}
Porosity	0.01
Volumetric heat capacity	2.10^{6} J m^{-3} K^{-1}

Figures

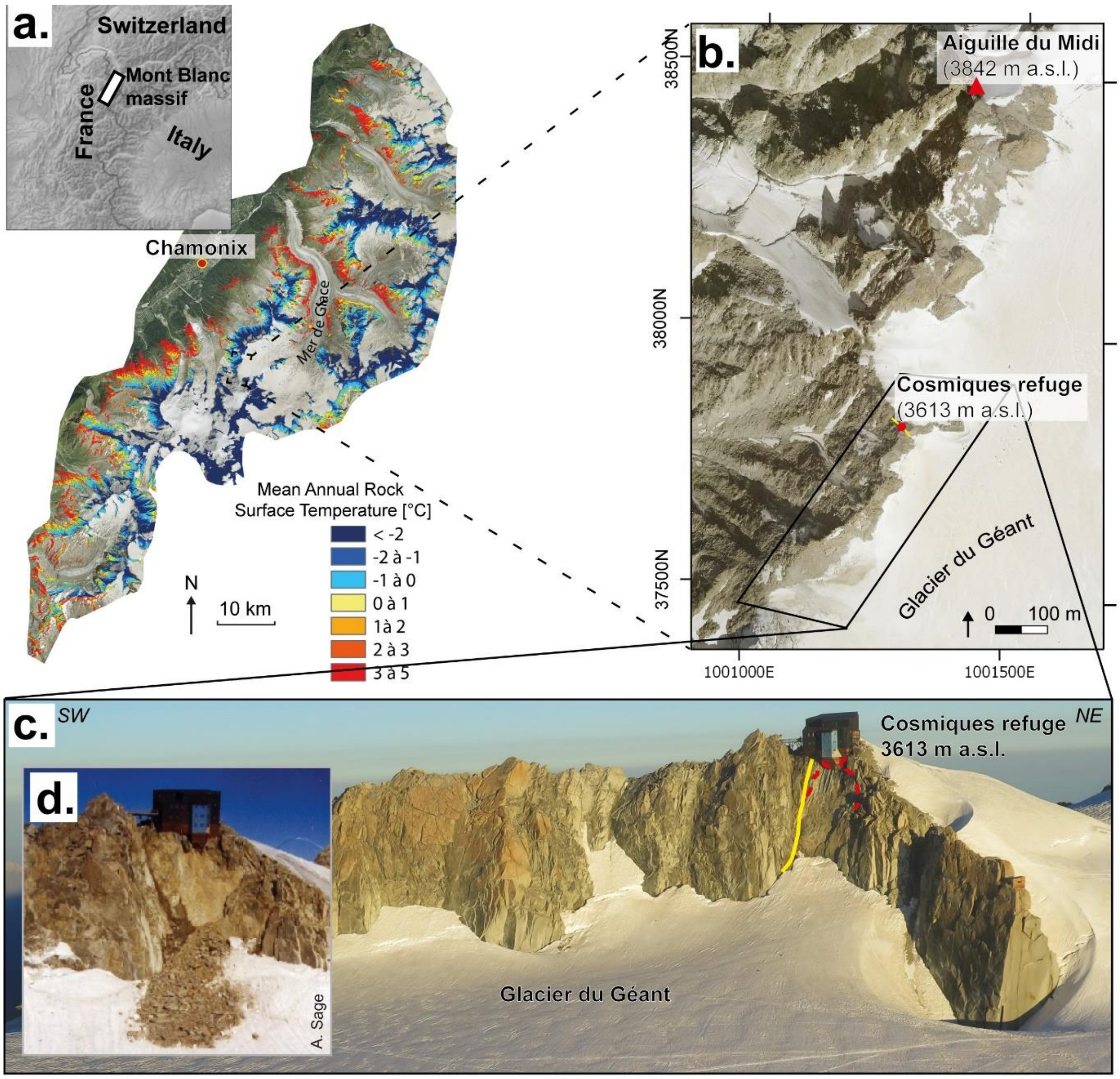

Figure 1. The Cosmiques refuge on the lower Cosmiques rock ridge (Mont Blanc massif, Western European Alps, France). **a.** The Mont Blanc massif (here, the French side) is largely affected by the permafrost (Magnin et al., 2015a). **b.** The lower Cosmiques ridge close to the Aiguille du Midi (3842 m a.s.l.). **c.** South-east face of the lower Cosmiques ridge seen from the glacier du Géant (Sept. 2016). **d**. The Cosmiques rockfall of August 1998 (~600 m^3).

Figure 2. Location of the temperature sensors and the ERT profile below the Cosmiques refuge. The labels COS-NW and COS-SE denote the position of the temperature sensors.

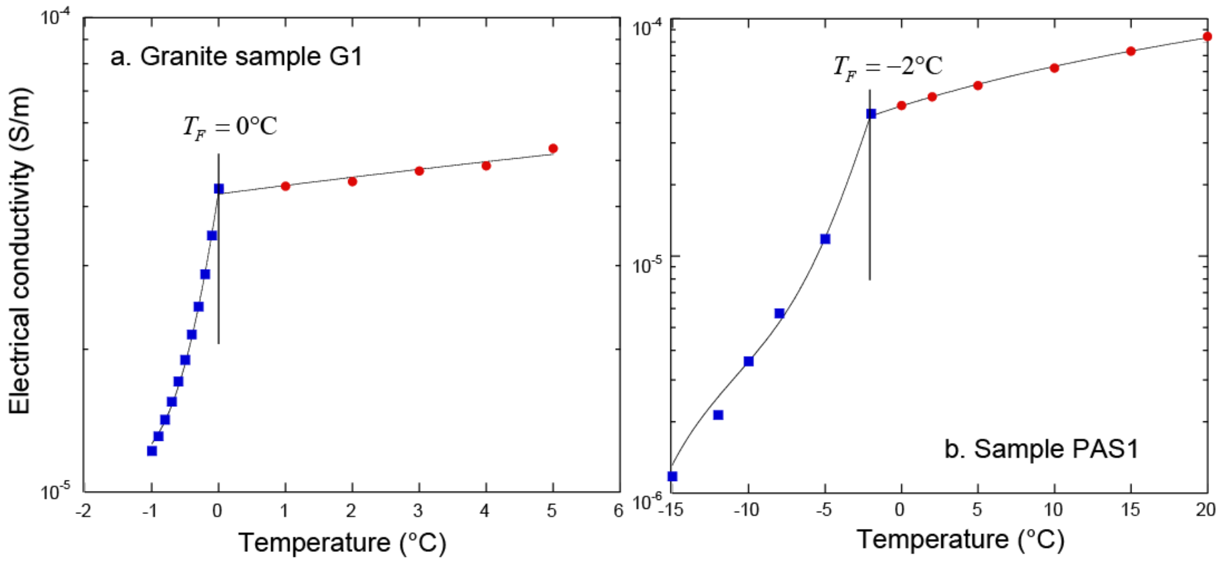

Figure 3. Electrical conductivity data versus temperature for two granite core samples from the Cosmiques rock ridge and fit of the data with the model from Duvillard et al. (2018). **a.** Granite sample G1 between -1 to +5°C ($T_F = 0°C$). The value of model parameters used to fit the measured data are T_C = -0.36°C, ϕ = 0.028, θ_r = 0.006, and $\sigma(T_0)$ = 8.8×10^{-5} S m^{-1}. **b.** Granite sample PAS1 between -15 to +20°C ($T_F = -2°C$). The value of the model parameters are T_C = -2.2°C, ϕ = 0.028, θ_r = 0.005, and $\sigma(T_0)$ = 9.3×10^{-5} S m^{-1}. In both cases, the symbols denote the experimental data (red above the freezing temperature and blue below the freezing temperature) while the plain lines correspond to the fit of the model.

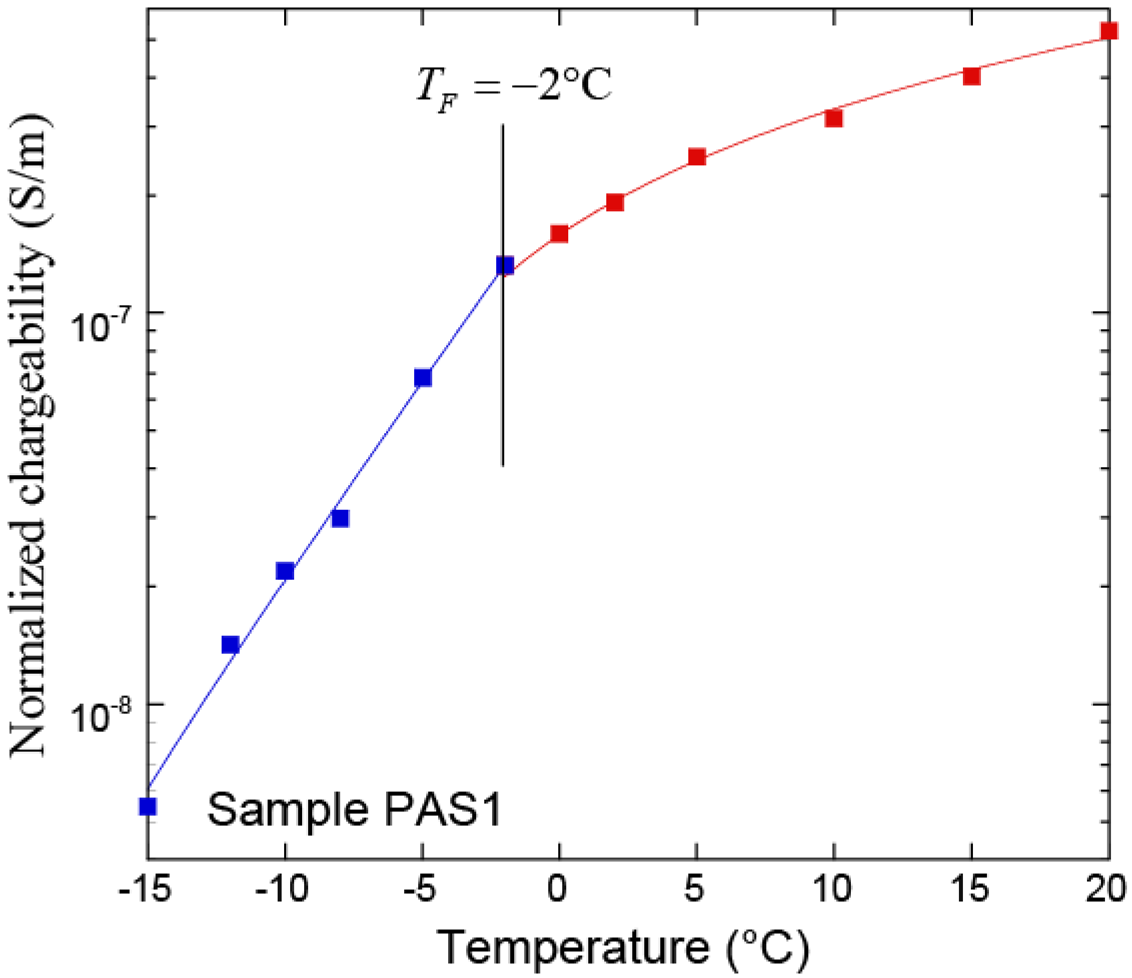

Figure 4. Normalized chargeability data versus temperature for the granite core sample PAS1 between -15 to +20°C ($T_F = -2°C$). The value of the model parameters are T_C = -5.4±0.7°C, ϕ = 0.028, θ_r = 0.001, $M_n(T_0)$ = 5.9×10^{-7} S m^{-1}, α_T = 0.028±0.0007 °C^{-1}. The symbols denote the experimental data (red above the freezing temperature and blue below the freezing temperature) while the plain lines correspond to the fit of the model.

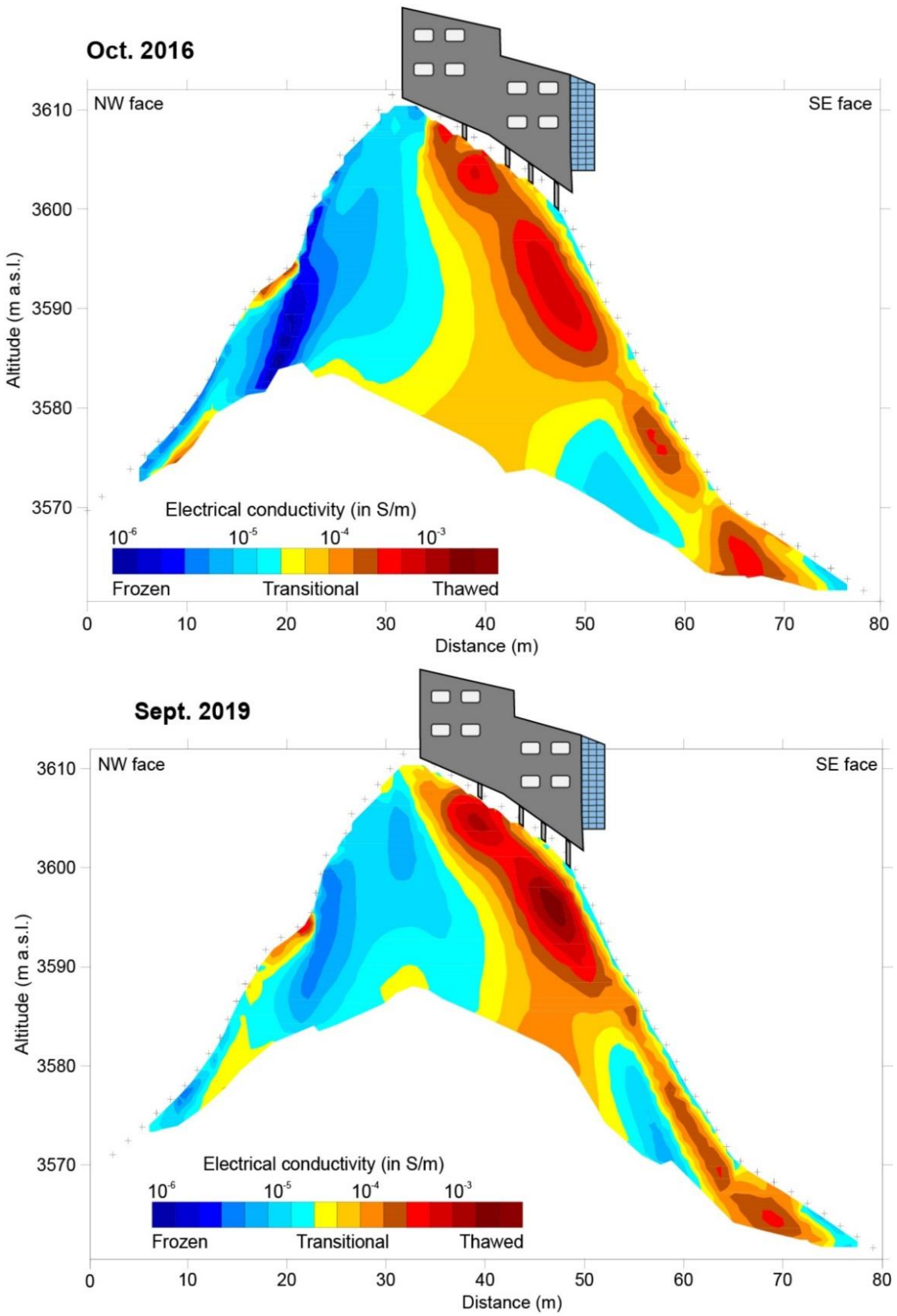

Figure 5. Electrical conductivity tomography (in S m^{-1}) of the rock ridge below the Cosmiques refuge in 2016 and 2019. We use cold colors for the low conductivity values presumed to correspond to the rock mass undergoing freezing conditions. The warm colors corresponds to the rock mass above freezing conditions.

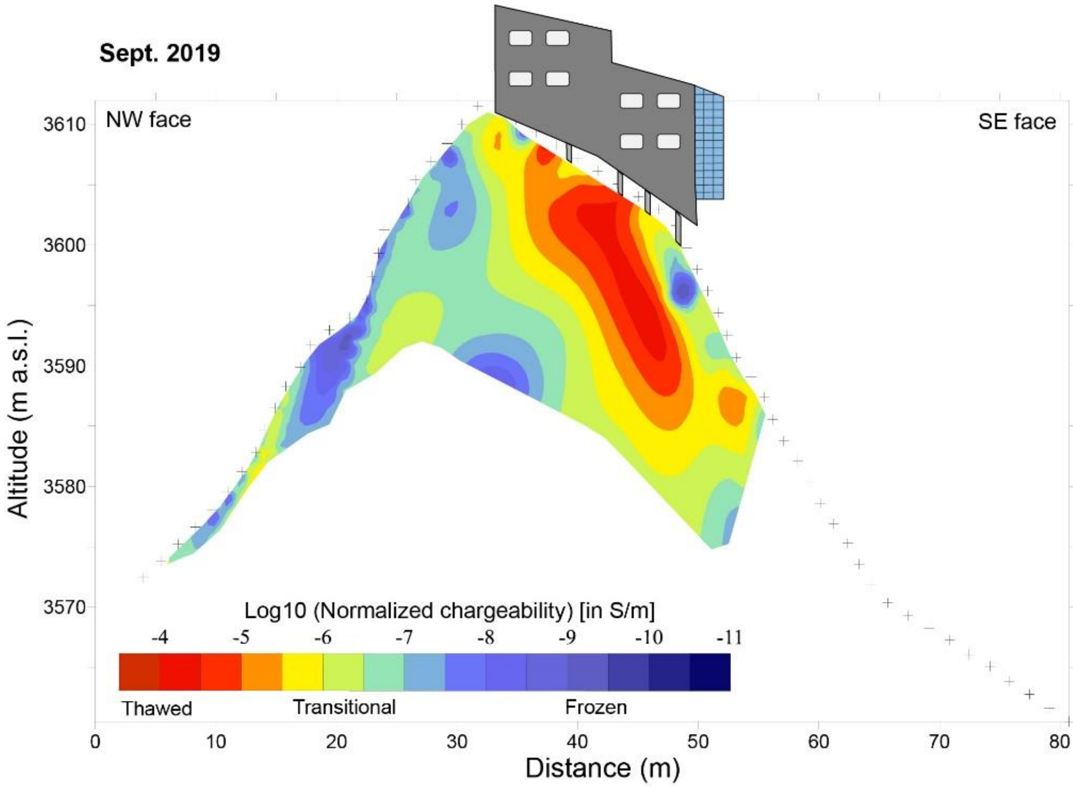

Figure 6. Normalized chargeability tomograms (in S m^{-1}) of the rock ridge below the Cosmiques refuge in 2019. Tomogram is smaller in SE face due to the lack of inverted data points.

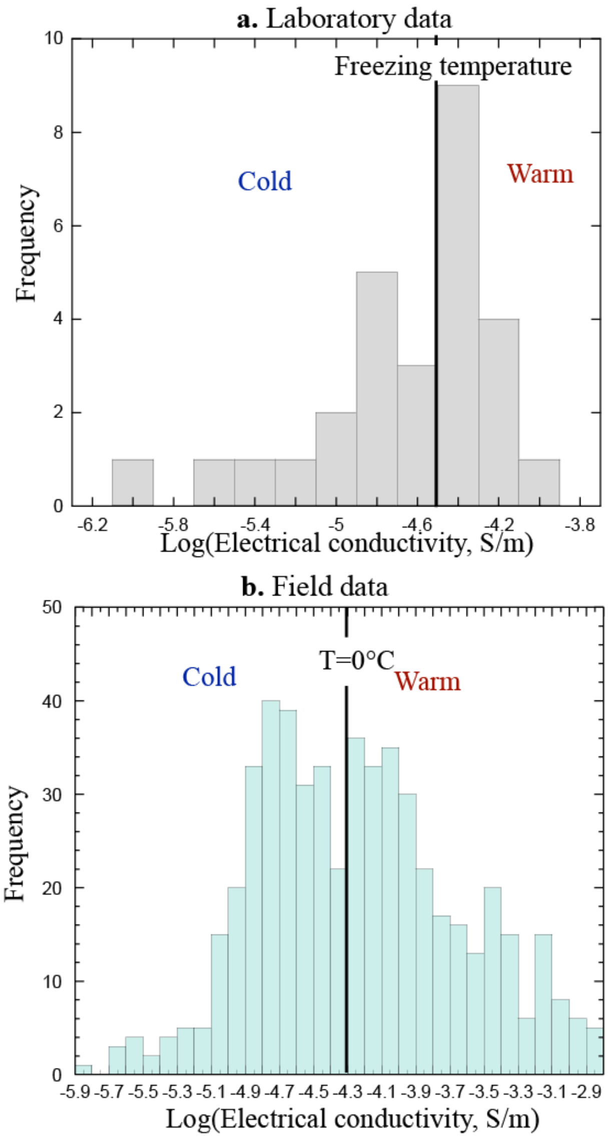

Figure 7. Distribution of the electrical conductivity. **a.** Laboratory data. **b.** 2016-Field data from the electrical conductivity tomogram. The observed minimum in the distribution is used to define the value of the electrical conductivity of the material at the freezing temperature. In the field data, we obtain $\sigma(T_F = 0°\mathrm{C}) = 5\times10^{-5}$ S.m^{-1} (obtained from the vertical plain line associated with the minimum in the conductivity distribution).

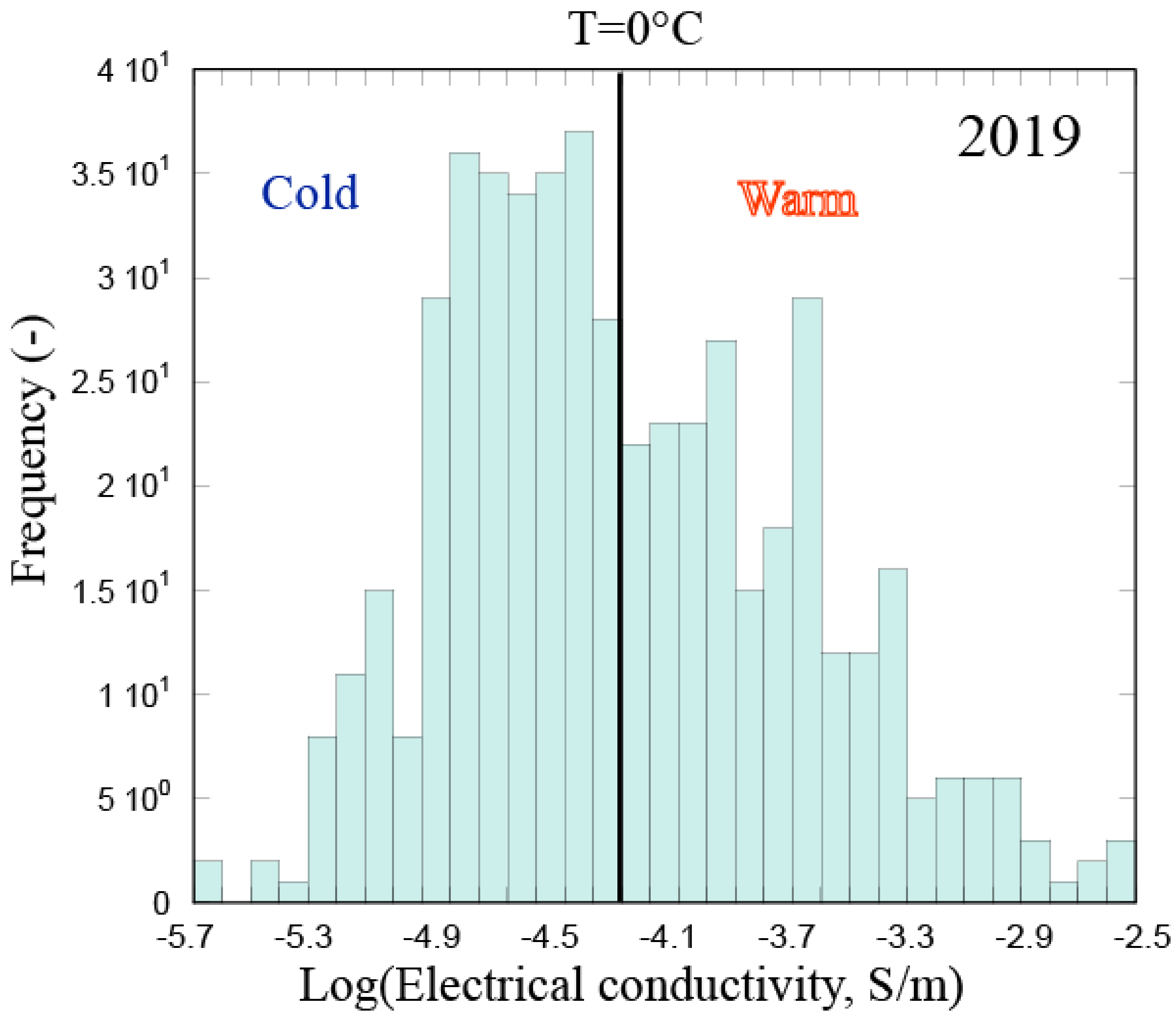

Figure 8. Distribution of the electrical conductivity for the 2019 field data. We observe a clear increase of the conductivity distribution with respect to 2016 (see Figure 7).

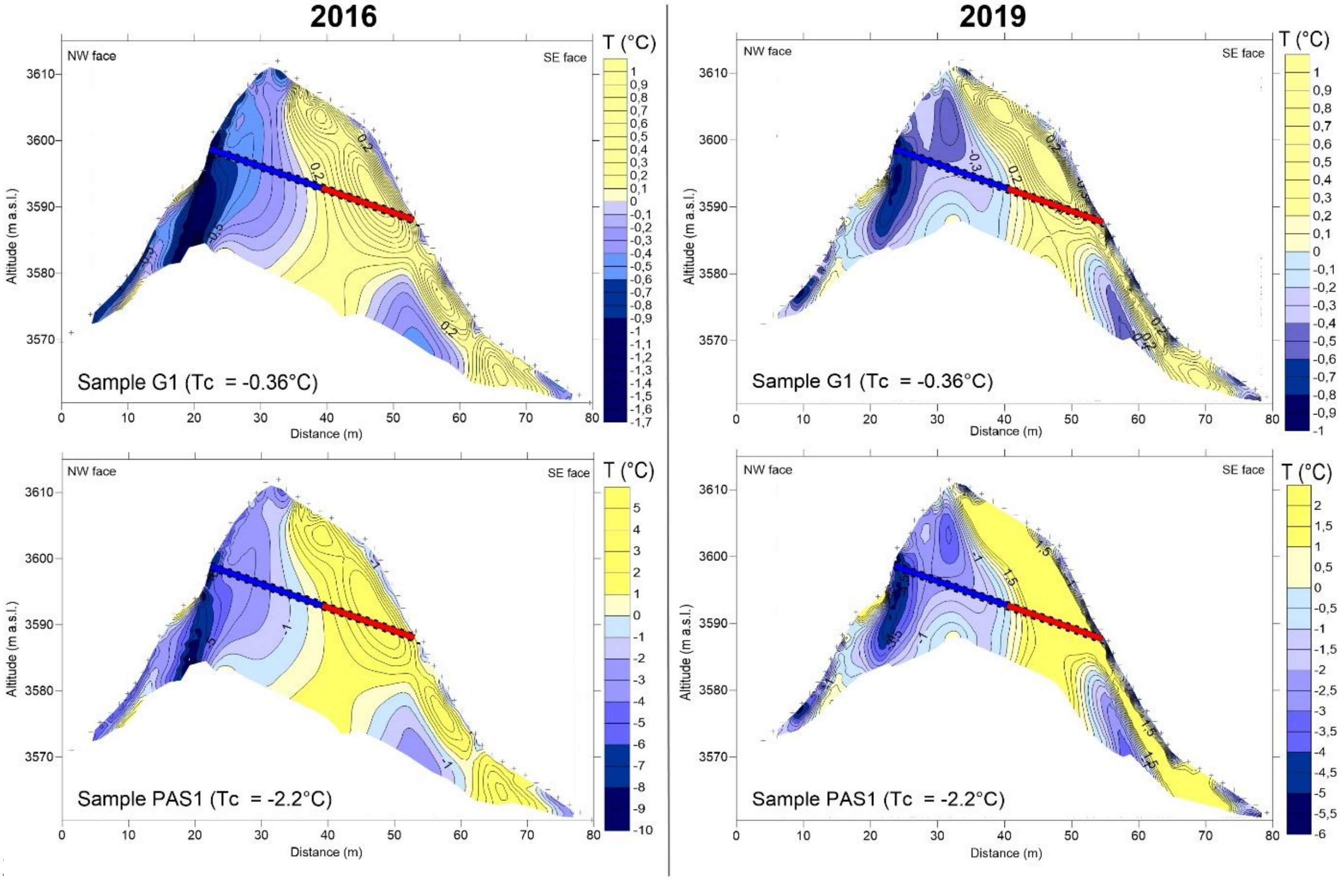

Figure 9. Distribution of the temperature determined from the electrical conductivity distribution for the 2016 and 2019 tomograms. **a.** Distribution obtained with the characteristic temperature $T_C = -0.4°\mathrm{C}$ and $T_C = -2.2°\mathrm{C}$. Permafrost is inferred below the NW face of the rock ridge. We also show the pseudo-horizontal section of length 32.75 m crossing the ridge and used for the numerical modeling of the temperature field. The blue portion of this profile denotes the frozen section while the red portion indicates the zone above the freezing temperature. Note the excellent agreement between the geophysical prediction and the numerical model.

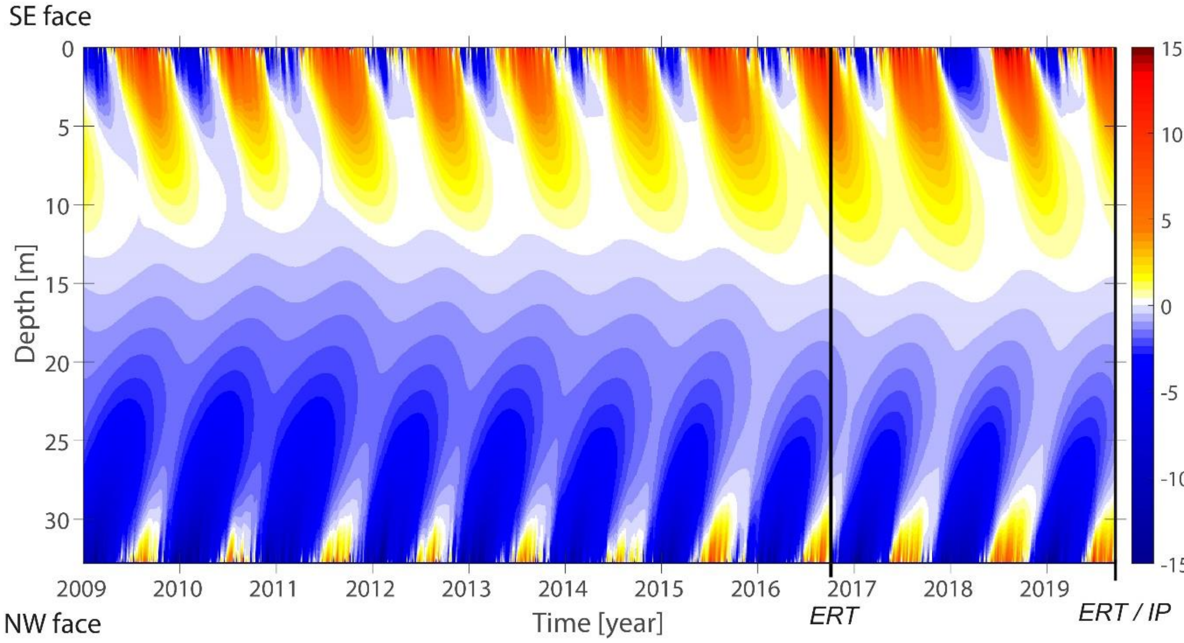

Figure 10. Modelled daily rock temperature along a horizontal section of 32.75 m crossing the ridge (as shown in Figure 9). The SE face of the rock ridge corresponds to the top of the section while the NW face corresponds to the bottom part of the section. The temperature distribution is modeled by applying the observed thermal boundary conditions as explained in the main text. The two vertical lines correspond to the acquisition dates (in 2017 and 2019) of the geophysical data (ERT stands for electrical resistivity tomography while IP stands for induced polarization). We see that a large portion of the ridge is expected to be frozen.

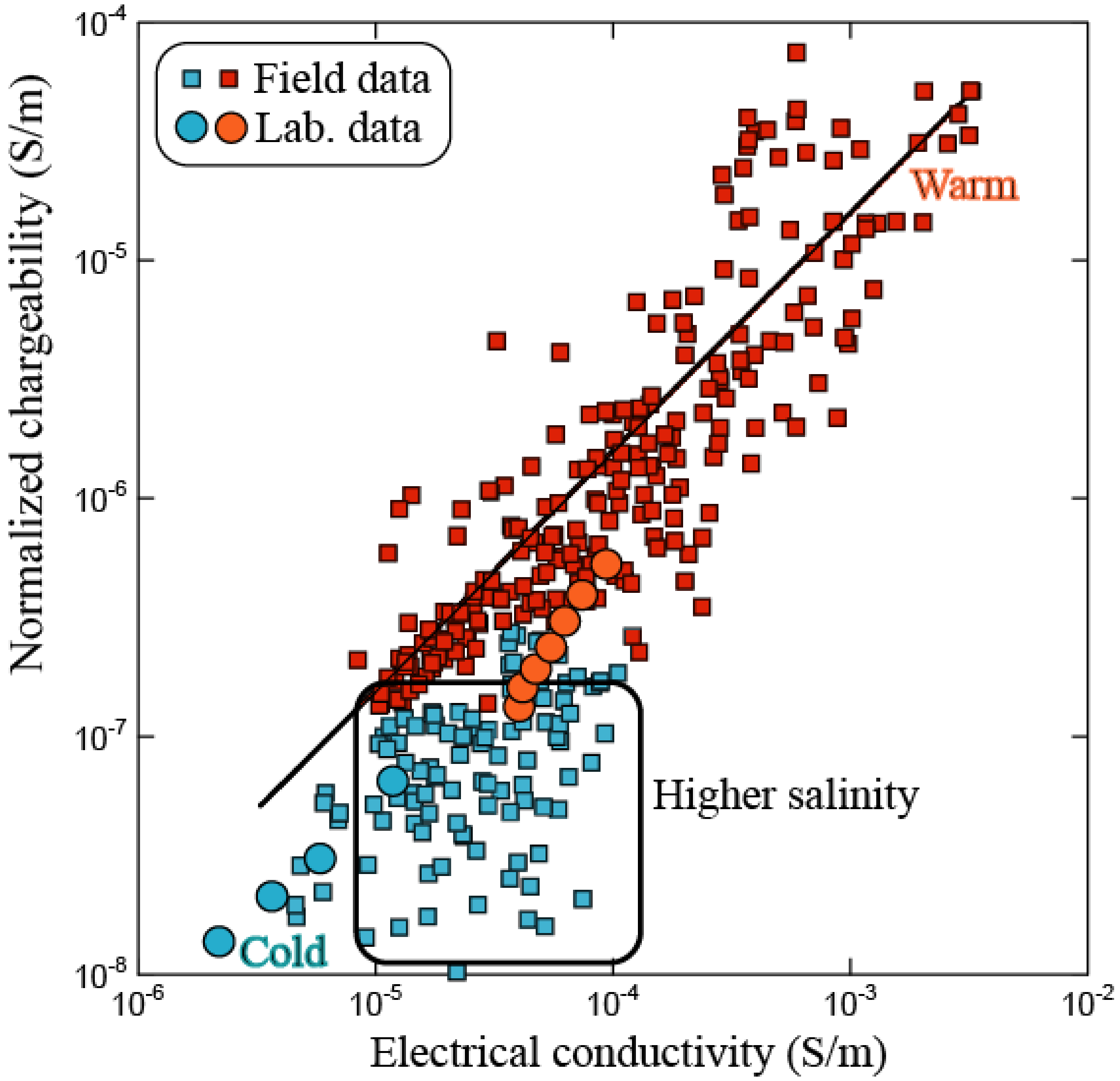

Figure 11. Normalized chargeability versus electrical conductivity. Comparison between the field and laboratory data (PAS1). The color code is blue for the cold values below the freezing temperature and red above the freezing temperature. The plain line corresponds to the best fit of the field data (with a slope of 0.016, r = 0.69). The small value of the slope (smaller than R = 0.10 indicates that conductivity is mostly dominated by the pore water contribution.